Human pollution exposure correlates with accelerated ultrastructural degradation of hair fibers

Gregoire Naudin[a], Philippe Bastien[a], Sakina Mezzache[a], Erwann Trehu[a], Nasrine Bourokba[a], Brice Marc René Appenzeller[b], Jeremie Soeur[a], and Thomas Bornschlögl[a,1]

[a]Advanced Research, L'Oréal Research & Innovation, 93601 Aulnay-sous-bois, France; and [b]Human Biomonitoring Research Unit, Luxembourg Institute of Health, 1445 Strassen, Luxembourg

Edited by David A. Weitz, Harvard University, Cambridge, MA, and approved July 29, 2019 (received for review March 15, 2019)

Exposure to pollution is a known risk factor for human health. While correlative studies between exposure to pollutants such as polycyclic aromatic hydrocarbons (PAHs) and human health exist, and while in vitro studies help to establish a causative connection, in vivo comparisons of exposed and nonexposed human tissue are scarce. Here, we use human hair as a model matrix to study the correlation of PAH pollution with microstructural changes over time. Two hundred four hair samples from 2 Chinese cities with distinct pollution exposure were collected, and chromatographic-mass spectrometry was used to quantify the PAH-exposure profiles of each individual sample. This allowed us to define a group of less contaminated hair samples as well as a more contaminated group. Using transmission electron microscopy (TEM) together with quantitative image analysis and blind scoring of 82 structural parameters, we find that the speed of naturally occurring hair-cortex degradation and cuticle delamination is increased in fibers with increased PAH concentrations. Treating nondamaged hair fibers with ultraviolet (UV) irradiation leads to a more pronounced cortical damage especially around melanosomes of samples with higher PAH concentrations. Our study shows the detrimental effect of physiological concentrations of PAH together with UV irradiation on the hair microstructure but likely can be applied to other human tissues.

air pollution | transmission electron microscopy | cortical damage

With the rise of industrialization and growing human mobility, environmental pollution due to industrial and transportation-related emissions and due to the dispersion of toxic chemicals has increased significantly during the last centuries with a detrimental impact on human health (1, 2). Although efforts are undertaken worldwide to reduce the emission of airborne, chemical, and soil pollutants, and although a reduced global exposure to, e.g., household air pollution and smoking can be observed from the 1990s on, the exposure due to ambient particulate matter and many other risk factors is still increasing globally (3). Household and ambient air pollution alone are a major cause of disease, where the main burden is on the Western Pacific and South East Asian regions, respectively. China, for example, has made much progress in increasing live expectancy and in decreasing the child mortality rate during the last 5 decades, but this rapid epidemiological change also comes with a sharp increase of noncommunicable diseases where ambient and household pollution being ranked fourth and fifth as the most important responsible risk factors (4). There is a growing body of evidence due to human biomonitoring methods with increasing sensitivity (5) showing a correlation between air pollution and disease (2, 6). In vitro experiments and in vivo correlations allow today to propose a causative relation between exposure to particulate matter (PM), production of reactive oxygen species, inflammation, and DNA damage explaining the correlation between PM exposure and increased mortality (7). Some pollutants, especially of the family of polycyclic aromatic hydrocarbons (PAHs) are phototoxic and in vitro experiments suggest in the case of skin an increased deleterious effect of simultaneous PAH pollution and ultraviolet (UV) exposure (8). However, despite the advancements in our understanding of pollution-related diseases, there is still a need to explore the links between pollution and subclinical impairment on human tissue (2). Here, we used human hair to better understand the structural impact of pollutants when incorporated in human tissue and exposed to naturally occurring wear and levels of UV light.

Due to the increased sensitivity of analytical methods such as chromatographic-mass spectrometry, hair is becoming a standard matrix for biomonitoring (9), closing the gap to the classically used matrices such as urine and blood together with other matrices such as breast milk and saliva (5, 10). Using human hair as a matrix has the advantage to provide integrated information on chronic exposure to pollution covering up to several months for each individual. Moreover, hair analysis allows for the detection of both parent pollutants and their metabolites, contrary to biological fluids usually used. Pollutants can enter the hair follicle via the blood stream or surrounding tissue and remain in the cortex of the differentiated hair matrix (11, 12). Today, different organic pollutants have been detected in hair such as polycyclic aromatic hydrocarbons (PAHs) and polychlorinated dibenzodioxins (PCDDs) coming among other sources from combustion. Also, different pesticides used in agriculture were found in hair such as organophosphates and organochlorines. In addition, polychlorinated biphenyls (PCBs) that were used as coolant liquids and plasticizers as well as polybrominated diphenyl ethers (PBDEs) widely used as

Significance

Air pollution via phototoxic polycyclic aromatic hydrocarbons (PAHs) is a major risk factor for human health. While in vitro observations and in vivo correlations suggest a detrimental effect of PAHs at physiological concentrations, in vivo observations of the structural impact of PAHs are scarce. Here, we use transmission electron microscopy on human hair fibers containing known concentrations of 25 biomarkers of PAH exposure. We show an increased structural degradation of the hair fiber over time, when increased PAH concentrations are present. Moreover, we show that exposure to UV radiation explains part of the increased damage in more contaminated fibers. Our results point toward possible detrimental effects in other human tissues at physiological concentrations of PAHs.

Author contributions: G.N., S.M., N.B., B.M.R.A., J.S., and T.B. designed research; G.N. performed research; B.M.R.A. contributed new reagents/analytic tools; G.N., P.B., E.T., and B.M.R.A. analyzed data; and G.N. and T.B. wrote the paper.

Conflict of interest statement: G.N., P.B., S.M., E.T., N.B., J.S., and T.B. are employees of L'Oréal.

This article is a PNAS Direct Submission.

[1]To whom correspondence may be addressed. Email: thomas.bornschloegl@rd.loreal.com.

This article contains supporting information online at www.pnas.org/lookup/suppl/doi:10.1073/pnas.1904082116/-/DCSupplemental.

Published online August 26, 2019.

flame retardants (9) can be detected in human hair. While hair grows and while the fiber ages over time, both the internal structure of the cortex as well as the integrity of the external cuticle become damaged due to environmental effects such as UV exposure, changes in humidity, or mechanical wear (13–15). To study the impact of pollution on this naturally occurring damage, we used transmission electron microscopy (TEM) to quantify microstructural changes along the hair fibers from 2 groups of women living in 2 cities with distinct air pollution profiles. In addition, we quantified the hair damage in dependence of the individual pollution profiles of subgroups and showed a link between increased hair damage and increasing concentrations of pollutants when exposed to UV light.

Differences in Cortical Hair Microstructure between Hair Samples from Cities with Different Air Pollution Profiles

China has recently developed a national air reporting system allowing hourly measurements of air pollutants such as particulate matter <2.5 μm ($PM_{2.5}$), particulate matter <10 μm (PM_{10}), sulfur dioxide (SO_2), nitrogen dioxide (NO_2), ozone (O_3), and carbon monoxide (CO). Data collected over several months during the year 2014 (16) allowed us to choose 2 different cities, Baoding and Dalian, that have different air pollution profiles but that are located on comparable latitude and elevation and also have similar climate conditions (17). Overall, the average concentration of $PM_{2.5}$ and of PM_{10} was higher in Baoding as compared to Dalian, in agreement with the air quality index of both cities (16, 17). In the framework of an already published study, we collected single strands of natural hair from 102 anonymized female volunteers from each city at the age of 25–45 y that gave a written consent (17). To compare the hair microstructure of the different samples, we cut a subregion of the hair fiber at a distance of 20 cm from the root corresponding to roughly 1.5 y of hair growth (18) and visualized the cuts using transmission electron microscopy (TEM; *Materials and Methods*). Fig. 1*A* shows a representative TEM image of such a cut of an individual hair fiber where the cuticle (cu) and the cortex (co) are visible. The arrows point to a cortical cell (c), which is delimited by the brighter cortical cell membrane complex (cmc) and which contains smaller macrofibers with roughly 0.5-μm diameter (19–21), melanin granules (me) and nuclear remnants (nr). Fig. 1 *B* and *C* show a representative image taken in the cortex of a hair fiber coming from Dalian and Baoding, respectively. For the hair sample coming from Dalian, only few white areas due to absent biological material are visible, while more of these zones are observed for the sample coming from Baoding. Such empty zones that are sometimes called vacuole or lacunae in the literature have been observed in chemically treated hair (22) and also in hair that has aged over time (15), while they are qualitatively less often observed in untreated, natural hair close to the root. To quantify the relative area of empty zones, we measured the area corresponding to a white signal using a threshold algorithm (Fig. 1*D* and *Materials and Methods*) and divided it by the total area of the taken image. The resulting cortical damage ratio measured on a representative subpopulation of 40 individuals coming from each city (see *SI Appendix* for sampling) is shown in Fig. 1*E*. The cortical damage ratio is significantly higher for hair fibers coming from Baoding as compared to the fibers collected in Dalian (5.1 ± 2.8% vs. 2.7 ± 3.2%, respectively). To contrast the observed damage on the hair cortex with the impact of bleaching procedures, we determined the damage ratio of a homogenized swatch of bleached Chinese hair, and we observed an increasing damage ratio with increasing bleaching intensities (*SI Appendix*, Fig. S1). In general, the observed empty zones can appear in different locations. They can be due to absent melanin granules, absent cellular remnants, or due to fractures appearing in the cmc. These alterations can either occur already in the hair in vivo or during sample preparation using the microtome, but they are in any case reminiscent of a locally degraded or mechanically less stable microstructure in the fiber. The increased damage ratio for hair samples coming from Baoding correlates with the increased air pollution profile as compared to Dalian. However, air quality is only one factor among others such as nutrition quality that contributes to the pollution profile of an individual. To quantify the link between an individuals' exposure to pollution and alterations in the hair microstructure, we grouped hair fibers having a similar pollution profiles and studied the correlated cortical damage.

Link between Pollution Subgroups and the Dynamics of Structural Changes in the Hair Cortex

Gas chromatography coupled with tandem mass spectrometry was used to analyze different parent PAHs and their metabolites within the first 12 cm of the individual hair samples, which was published before (17). This gives access to the pollution profile of each person averaged over a 1-y exposure (18). When focusing only on PAH pollution, we can describe the dataset as a n × m

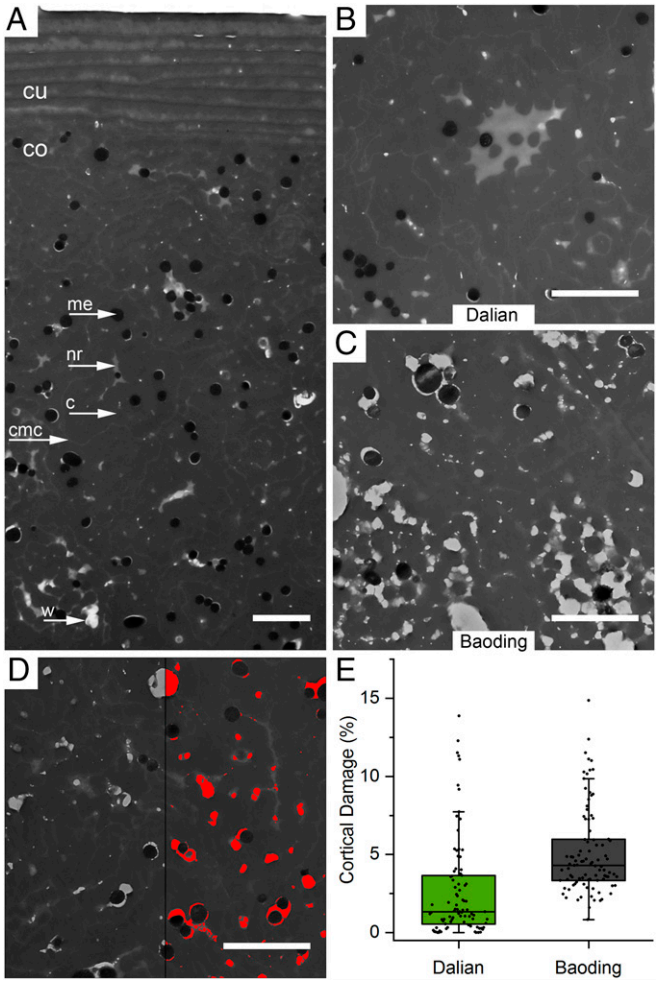

Fig. 1. Visualization of hair structure and quantification of cortical damage. (*A*) Representative TEM image of the cuticle (cu) and cortex (co) of a human hair. The white areas (w) indicate regions without biological material reminiscent of damaged regions. (*B*) Image of human hair cortex originating from Dalian and cut at a distance of 20 cm from the root. (*C*) Image of human hair cortex originating from Baoding and cut at a distance of 20 cm from the root. (*D*) Visualization of white areas via a thresholding algorithm (colored red on the right). (*E*) Boxplots of the area occupied by white regions divided by the total area of the image (cortical damage ratio) for Dalian and Baoding, respectively. Each point corresponds to one fiber. $n = 40$ independent fibers per city. (Scale bars: 2 μm.)

matrix X, where the columns $m = 1,2,3 \ldots$ M denote the type of PAH pollutant and the rows $n = 1,2,3 \ldots$ N denotes the individual hair sample. The value $X_{i,j}$ denotes then the logarithm of the measured concentration of the pollutant. A partial least squares discriminant analysis (PLS-DA) based on the X log transformed pollutant concentration matrix was performed to discriminate between the 2 cities (17). PLS-DA, as a factorial method, allows us to visualize the data in a reduced dimensional space. Based on the first 2 dimensions, the X matrix can be factorized as

$$X = t_1 p_1^{\mathrm{T}} + t_2 p_2^{\mathrm{T}} + R,$$

where the scores t_1 and t_2 are vectors with dimension of the individual hair samples N and the loadings p_1 and p_2 are vectors with dimension M of the number of analyzed PAHs, the matrix R being the residual matrix associated to the information not taken into account by the 2 first PLS components. The importance of a component is reflected by the proportion of the total inertia "explained" by this factor. In our case, the first component explains more than 45% of the total inertia of the pollution profiles, which is significant with regard to the number of PAH descriptors, and the first factorial plane about 53% of the total inertia. As shown on the biplot representation (*SI Appendix*, Fig. S2*A*), the PAH descriptors are grouped together on the right part of the first component. Note that for our dataset a similar result is obtained when using a nonsupervised principal component analysis (PCA) (*SI Appendix*, Fig. S2*C*). Thus, the first principal component can be interpreted as a pollution intensity axis, with t_1, the projection of the individuals on this component, as a global score of pollution. Fig. 2*A* shows the histogram of individual samples for each pollution intensity, which we get by using an equidistant binning along the first principal component axis of the PLS-DA. Samples in each of these bins have a comparable average pollution profile with increasing average logarithmic pollutant concentrations along the axis. To get sufficient different hair samples in each subgroup, we regrouped the rare extreme cases into groups 1 and 14. Along the first principal component axis, the 2 cities are differently distributed, individuals at the left of the axis mostly coming from Dalian have an overall low concentration of the different pollutants, while individuals at the right of the axis have comparably high concentrations of PAH and its metabolites. Hair samples of the different subgroups were recombined and reanalyzed (*SI Appendix*) with the image analysis method described above. Fig. 2*B* shows the damage ratio of the cortex for the 14 different subgroups. We can observe a significant increase of the hair cortex damage ratio from group 6 on. Thus, independent of the city of origin, hair samples with a pollution profile equal or higher than group 6 already show a significantly increased damage ratio in the hair cortex after 1.5 y of hair growth. To study the microstructural differences between a less contaminated and a contaminated group over time and in more detail, we pooled 50 samples coming from the groups 2–5 into a low pollution profile group (blue box in Fig. 2*B*), and 50 samples coming from the groups 10–13 into a high pollution profile group (red box in Fig. 2*B*). The mean concentrations of all detected PAHs for both subgroups are given in *SI Appendix*, Table S1. First, we wanted to quantify the dynamics of microstructural degradation over time of hair growth in the cortex of both contamination groups. To this end we prepared transversal cuts of single hair fibers from both groups at 3 positions along the hair fiber: directly at the root, at 20 cm, and at 40 cm distance. This corresponds to a nascent hair fiber and to an age of 1.5 y and 3 y, respectively. We took one image at a randomly chosen position within the cortex of each fiber (*SI Appendix*) and quantified the damage ratio in the cortex as explained in Fig. 1*E*. The results are shown in Fig. 2*C*. If we approximate linearly the increase of the damage ratio over time, we can estimate a higher speed of naturally occurring cortical damage in the contaminated group as compared to the less contaminated group (2.7% per year vs. 0.67% per year, respectively) with an initial damage ratio measured already at the root of 0.7 ± 0.4% and 0.8 ± 0.6% for the contaminated and less contaminated group, respectively. This confirms the observation of a more damaged cortex after 1.5 y of hair growth for fibers coming from Baoding as compared to Dalian (Fig. 1*E*) but is now specifically correlated with the individual hair fiber pollution signatures. A more detailed analysis of the cortex damage ratio at 3 different positions of the hair fibers for the 14 subgroups is shown in *SI Appendix*, Fig. S3. In a next step, we counted the number of cuticle layers for both contamination groups, which are known to naturally decrease due to mechanical wear and other environmental cues over time (13, 15). The result is shown in Fig. 2*D*. If we approximate the speed of cuticle layer detachment with a linear decrease, we find a faster decrease for the contaminated group compared to the less contaminated group (2 layers per year vs. 1 layer per year, respectively).

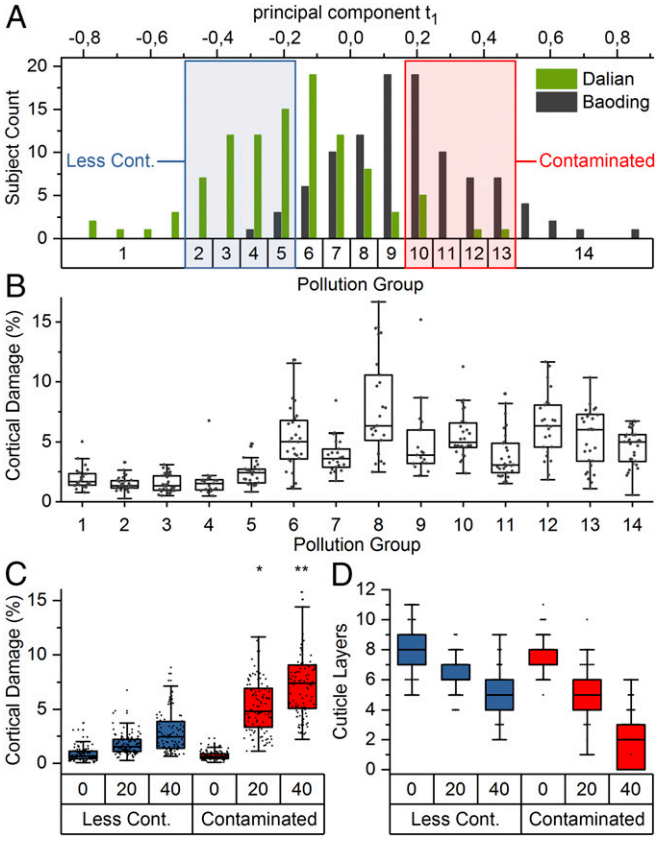

Fig. 2. Definition of pollution groups and quantification of damage. (*A*) Histogram of individual hair samples falling into different pollution subgroups (lower axis) defined along the first principal component of a PLS-DA done on the PAH concentrations of individual hair samples (upper axis). The overall pollution profile increases along the axis. The groups were pooled into a less contaminated (blue square) and a contaminated subgroup (red square). (*B*) Boxplots of the cortical damage ratio observed at 20 cm distance of hair fibers from the 14 different subgroups. $n = 25$. (*C*) Cortical damage of the less contaminated and contaminated groups measured at 3 different distances along the hair fiber corresponding to nascent fiber (0 cm) and 1.5 y (20 cm) as well as 3 y of hair growth (40 cm). $n = 100$ for each condition. (*D*) Counts of visible cuticle layers for both groups measured at 0, 20, and 40 cm distances along the hair fiber. $n = 60$.

Specification of Microstructural Changes Using Blinded Expert Scoring

The above methods to quantify the damage of the hair cortex and cuticle are objective, but do not give any information about the specific type of damage nor the exact damage localization within the hair. To get insight into these parameters, we developed a blinded scoring protocol based on a set of 82 yes-no scores. The entire list of scores is given in the *SI Appendix*, Fig. S4*B*, and a few scores are visualized in Fig. 3. For example, one score is given for the presence of structural defects close to the melanosomes (sd1 in Fig. 3) and one for defects at the cortical cell membrane complex (sd2). We answered the scores for fiber sections taken in a region close to the root, one region at 20 cm, and one region at 40 cm distance on 40 hair fibers from both contamination groups. For yes answers we chose the value 1, and for no answers the value 0, giving equivalent weight to every question. A PCA on the scoring dataset is shown in the *SI Appendix*, Fig. S4*A*, where the parameter of sample origin was unblinded after scoring. In general, the spread of the scoring values for the first 2 principal components increases with increasing distance from the root for both contamination groups, as it is expected for increasing overall damage over time. In addition, the spread of the scoring values collected at 20 and 40 cm along the hair fiber is larger for the contaminated group as compared to the fiber with similar age in the less contaminated group (*SI Appendix*, Fig. S4*A*). This is in good agreement with the increased cortical damage ratio of the contaminated vs. less contaminated group shown in Fig. 2*C* and the decreasing amount of cuticle layers (Fig. 2*D*) but includes now additional information about the types of damage. To highlight the damage scores with the most impact on the distribution of points in the first 2 principal components, we list the scores with a loading vector having a length larger than 0.1 (*SI Appendix*, Fig. S4*B*). Among these scores we find changes occurring at the melanosomes and their adjacent zones such as a changed texture (sd3 in Fig. 3), or complete disappearance of melanosomes (sd4 in Fig. 3) with high loadings. Also, a well-preserved cmc in the cortex (is1 in Fig. 3) as well as cracks and holes appearing in between the cortical cells (sd2 in Fig. 3) have a large influence on the PCA distribution and explain the increased amount of empty areas in older or more contaminated fibers. Within the cuticle, the presence of vacuoles (sd5 in Fig. 3) related to fractures in the endocuticle have a major influence on the distribution of pollution and age groups in the PCA. In general, the scores with an important loading vector (listed in the *SI Appendix*, Fig. S3*B*) are more related to zones of the hair matrix and the cmc and less to keratinized zones of the hair although questions, e.g., about structural changes of the microfibrils were included in the 82 scores. These damages are reminiscent of damages occurring during UV exposure and chemical hair treatment such as bleaching routines (*SI Appendix*, Fig. S1) and point toward a deleterious effect of photoreactive pollutants together with UV exposure. To test the impact of UV irradiation alone, we exposed hair from the root level containing different pollution profiles to controlled amounts of UV irradiation.

Mechanistic Link between Pollution Enhanced Hair Structure Degradation and UV Exposure

To test the influence of UV irradiation on hair samples with different pollution profiles under controlled humidity conditions,

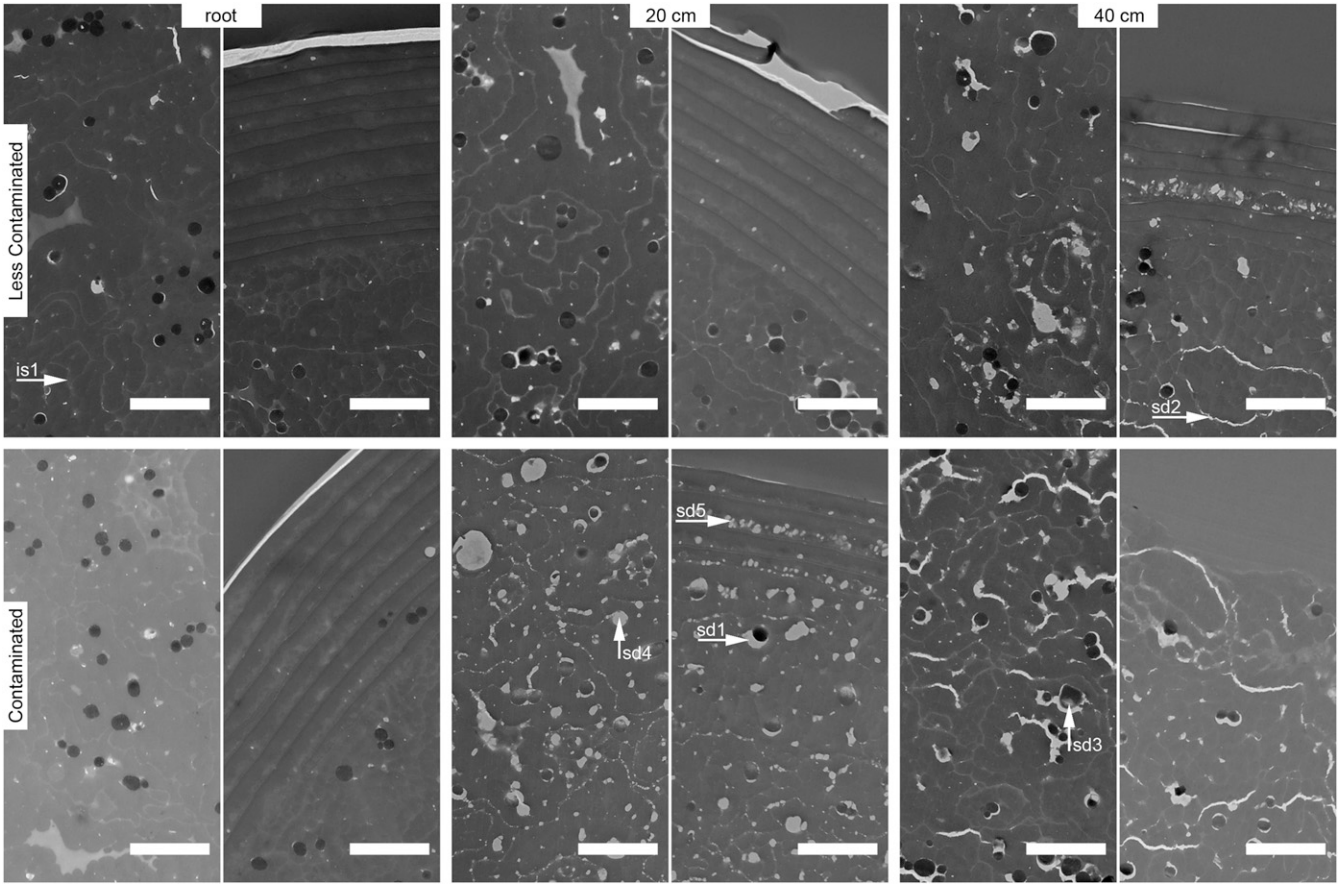

Fig. 3. Images of the cuticle and cortex from hair coming from the less contaminated group (*Upper*) and the contaminated group (*Lower*) taken at different distances along the hair fiber such as root (first column), 20 cm (second column), and 40 cm (third column). (Scale bars: 2 μm.)

we exposed the roots of 200 hair fibers from both contamination groups to different doses of UV irradiation using a Xenotest (*Materials and Methods*). In brief, the hair fibers are exposed to UV and visible light irradiation at wavelengths above 300 nm with an irradiance of 45 W/m^2 at 60% humidity and 35 °C for 4, 6, and 8 d nonstop. The dose corresponding to our 8-d treatment of 30 MJ(m)$^{-2}$ is roughly equivalent to a nonstop daylight exposure in China for 60 d (23, 24). Fig. 4*A* shows the results of the cortical damage analysis for the different treatments. Before any UV treatment, the cortical damage ratios of both contamination groups are again at 0.8 ± 0.4% and 0.7 ± 0.3% (Fig. 4*A*, 0D) as observed in Fig. 2*C*. For both groups, an increase in the damage ratio can be observed after 4 d of UV treatment, and the damage ratio after 8 d of UV treatment is significantly higher for the contaminated group as compared to the less contaminated group (3.9 ± 1.1% vs. 1.4 ± 0.9%). This indicates that at least part of the naturally observed cortical damage can be explained by UV-induced degradation of the hair fiber. Part of the overall cortical damage ratio comes from zones close to the melanosomes as shown in Fig. 4*B*. There, 2 randomly chosen images of melanosomes from less contaminated as well as the contaminated fibers are shown without any treatment (root) and after 8 d of UV exposure using the Xenotest (root + UV8D). Comparing the images of the less contaminated and the contaminated group with 8 d of UV treatment, one can distinguish the larger empty white zones around the melanosomes in the contaminated group as well as a change in texture of the melanosomes. To visually compare this damage to the damage observed in naturally exposed and growing hair, we also show images of the less contaminated and contaminated group after 1.5 y (20 cm) and 3 y (40 cm) of hair growth.

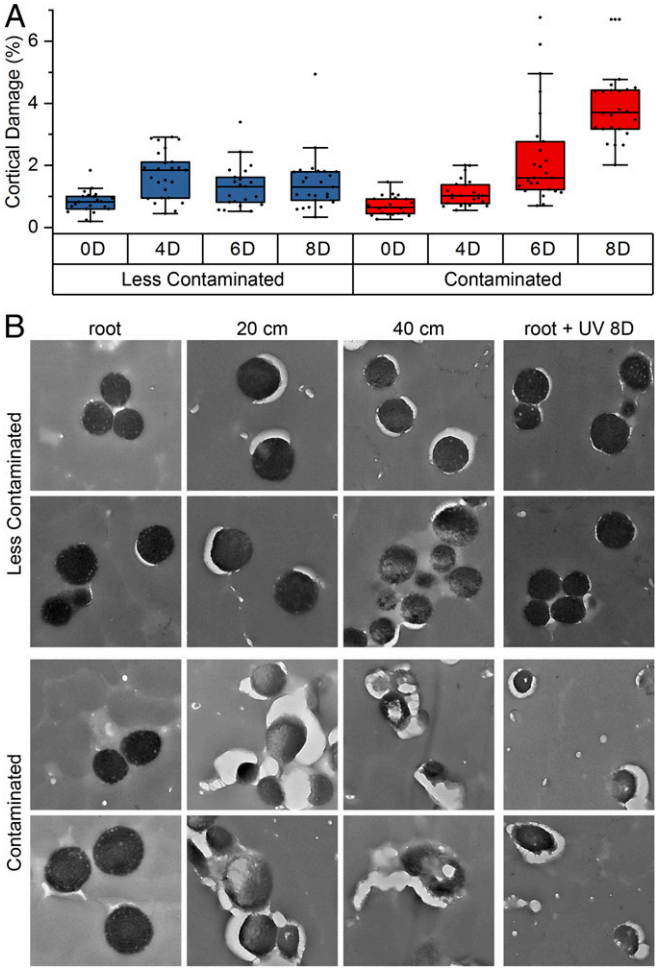

Fig. 4. Cortical damage and UV exposure. (*A*) Cortical damage ratio calculated for at least 20 independent fibers per condition for both contamination groups, before (0D) and after 4, 6, and 8 d of light irradiation. (*B*) Images of melanosomes in the cortex of untreated hair from the contaminated and less contaminated group at the root, 20 cm, and at 40 cm of untreated hair as well as hair from the root region treated with UV irradiation for 8 d. (Image size: 2 μm.)

Discussion

The present work shows that the naturally occurring damage of the hair cuticle and the cortex appears faster in hair fibers with higher average PAH concentrations, and that initially less-damaged fibers with increased PAH contamination show increased damage after UV treatment. In our study, we only focused on PAHs, which are the most prominent group of photoreactive pollutants. We cannot exclude additional correlations with other pollutants, e.g., originating from the same sources of production than PAHs, which could possibly be present in the hair fiber (except for nicotin and cotinine; ref. 17). However, the shown correlation between PAH concentration and UV-induced photo damage indicates a major causative contribution of PAHs in the degradation process. From different in vitro studies it is known that UV absorption by PAHs leads to exited states and subsequent production of reactive oxygen species (ROS) that have the ability to alter DNA, proteins, and cell membrane components, and can finally lead to decreased cell viability (5, 25–27). In vitro studies have shown that the detrimental effects linked to the photoreactivity of PAH and mainly UVA and long UVA irradiation already occur at physiological concentrations measured in different matrices for different PAHs in the range of 1 to 1,000 ng/g (8, 27, 28). Here, we observe to our knowledge for the first time that physiological concentrations of PAHs measured in hair between 0.2 and 200 ng/g are correlated with pronounced structural alterations in vivo. Thus, one hypothesis that could explain the accelerated cortical damage of the contaminated group is via UV-induced production of reactive PAH intermediates and ROS in the hair (13, 25). It would be interesting in the future to quantify the individual impact of a pollutant on the matrix, which likely depends on its photoreactivity and relative concentration in the fiber. Studying the effect of PAHs and UV light on the hair matrix could therefore help to better understand the known photo-enhanced toxicity of different PAHs and their impact on different phototoxicity models (29). A causative action of PAH, their metabolites, and UV-induced ROS would also explain our observation of mainly degraded cellular remnants in the matrix and the cmc containing lipids, protein, and DNA, while the compact macrofibers seem unaltered in our TEM images. In addition, the melanosome texture shows higher structural alterations in PAH-containing fibers, indicating an additional detrimental effect of UV on melanin when PAHs are present. This could be explained by a preferential accumulation of PAHs in the hair melanin, based on the observation that some PAHs are known to colocalize with melanin-rich tissues (30). Therefore, UVA irradiation would on one hand via photoactivation of PAHs lead to local production of ROS that are known to bleach hair via melanin degradation. However, UVA irradiation via photoactivation of the melanin itself could lead to a local increase of superoxide concentrations. Globally, the overall observed damage will likely only have a small impact on hair integrity and mechanics, which is dominated by the macrofibers, while the increased reduction of the cuticle might have a visible impact on hair appearance.

In this paper, we quantified the structural impact of PAH pollution on the hair matrix, but one could expect similar deleterious effects in other human tissues such as the skin (31) if photoreactive pollutants in physiological concentrations are present. For example, the deleterious effect of UV irradiation on PAH

contaminated, reconstructed human in vitro skin was already shown (8), which could be quantified by our method in the future to allow further insight in the underlying mechanisms.

Materials and Methods

Sampling and Image Acquisition. The sampling procedures used for the Figs. 1, 2, and 4 are detailed in *SI Appendix*, Figs. S5–S7 respectively. Details for the sample preparation and image acquisition are given in *SI Appendix, Supplementary Information Text* and Fig. S8. For all experiments, sample preparation for TEM observations was kept similar.

Damage Ratio and Cuticle Thickness Determination. To calculate the damage ratio, an algorithm based on the Multi Otsu Thresholding method was used on images after background subtraction using a rolling ball algorithm (diameter 50 pixels). Five pixel families were defined; the damage ratio expresses the area ratio between the last pixel family (corresponding to the brightest pixels) and the entire image area. To count the number of cuticle layers, a 60-pixel large profile was drawn across the cuticle and the intensity peaks corresponding to each cuticle layer were counted. Values given in the text are mean ± SD.

Xenotest. Sixteen fibers from nondamaged root regions of each individual of the less contaminated and contaminated group were randomly chosen and grouped together in 4 swatches. The swatches were mounted on a Xenotest chamber (Atlas, Xenothest alpha) and exposed to light irradiation using a Xenochrome 300 Filter corresponding to UV and visible light starting at 300 nm for different durations.

ACKNOWLEDGMENTS. We thank R. Gael for performing the Xenotest and L. Marrot, B. Bernard, and N. Baghdadli for helpful discussions.

1. A. Prüss-Ustün *et al*., Diseases due to unhealthy environments: An updated estimate of the global burden of disease attributable to environmental determinants of health. *J. Public Health (Oxf.)* **39**, 464–475 (2017).
2. P. J. Landrigan *et al*., The Lancet commission on pollution and health. *Lancet* **391**, 462–512 (2018).
3. M. H. Forouzanfar *et al*.; GBD 2015 Risk Factors Collaborators, Global, regional, and national comparative risk assessment of 79 behavioural, environmental and occupational, and metabolic risks or clusters of risks, 1990-2015: A systematic analysis for the global burden of disease study 2015. *Lancet* **388**, 1659–1724 (2016).
4. G. Yang *et al*., Rapid health transition in China, 1990-2010: Findings from the global burden of disease study 2010. *Lancet* **381**, 1987–2015 (2013).
5. J. Angerer, U. Ewers, M. Wilhelm, Human biomonitoring: State of the art. *Int. J. Hyg. Environ. Health* **210**, 201–228 (2007).
6. A. Valavanidis, K. Fiotakis, T. Vlachogianni, Airborne particulate matter and human health: Toxicological assessment and importance of size and composition of particles for oxidative damage and carcinogenic mechanisms. *J. Environ. Sci. Health C Environ. Carcinog. Ecotoxicol. Rev.* **26**, 339–362 (2008).
7. P. Møller *et al*., Oxidative stress and inflammation generated DNA damage by exposure to air pollution particles. *Mutat. Res. Rev. Mutat. Res.* **762**, 133–166 (2014).
8. J. Soeur *et al*., Photo-pollution stress in skin: Traces of pollutants (PAH and particulate matter) impair redox homeostasis in keratinocytes exposed to UVA1. *J. Dermatol. Sci.* **86**, 162–169 (2017).
9. B. M. R. Appenzeller, A. M. Tsatsakis, Hair analysis for biomonitoring of environmental and occupational exposure to organic pollutants: State of the art, critical review and future needs. *Toxicol. Lett.* **210**, 119–140 (2012).
10. M. Esteban, A. Castaño, Non-invasive matrices in human biomonitoring: A review. *Environ. Int.* **35**, 438–449 (2009).
11. F. Pragst, M. A. Balikova, State of the art in hair analysis for detection of drug and alcohol abuse. *Clin. Chim. Acta* **370**, 17–49 (2006).
12. R. C. Duca, E. Hardy, G. Salquèbre, B. M. Appenzeller, Hair decontamination procedure prior to multi-class pesticide analysis. *Drug Test. Anal.* **6** (suppl. 1), 55–66 (2014).
13. W.-S. Lee, Photoaggravation of hair aging. *Int. J. Trichology* **1**, 94–99 (2009).
14. J. M. Marsh *et al*., Advanced hair damage model from ultra-violet radiation in the presence of copper. *Int. J. Cosmet. Sci.* **37**, 532–541 (2015).
15. S. Thibaut *et al*., Chronological ageing of human hair keratin fibres. *Int. J. Cosmet. Sci.* **32**, 422–434 (2010).
16. R. A. Rohde, R. A. Muller, Air pollution in China: Mapping of concentrations and sources. *PLoS One* **10**, e0135749 (2015).
17. P. Palazzi *et al*., Exposure to polycyclic aromatic hydrocarbons in women living in the Chinese cities of BaoDing and Dalian revealed by hair analysis. *Environ. Int.* **121**, 1341–1354 (2018).
18. A. Rook, R. Dawber, *Diseases of the Hair and Scalp*, A. Rook, R. Dawber, Eds. (Blackwell Scientific Publications, 1991).
19. C. R. Robbins, *Chemical and Physical Behavior of Human Hair* (Springer New York, 2013).
20. T. Bornschlögl *et al*., Keratin network modifications lead to the mechanical stiffening of the hair follicle fiber. *Proc. Natl. Acad. Sci. U.S.A.* **113**, 5940–5945 (2016).
21. J. E. Plowman, D. P. Harland, S. Deb-Choudhury, *The Hair Fibre: Proteins, Structure and Development* (Springer Singapore, 2018).
22. H. J. Ahn, W.-S. Lee, An ultrastuctural study of hair fiber damage and restoration following treatment with permanent hair dye. *Int. J. Dermatol.* **41**, 88–92 (2002).
23. L. Wang *et al*., Measurements and cloudiness influence on UV radiation in Central China. *Int. J. Climatol.* **34**, 3417–3425 (2014).
24. H. Liu *et al*., Two ultraviolet radiation datasets that cover China. *Adv. Atmos. Sci.* **34**, 805–815 (2017).
25. H. Yu *et al*., Photoirradiation of polycyclic aromatic hydrocarbons with UVA light–A pathway leading to the generation of reactive oxygen species, lipid peroxidation, and dna damage. *Int. J. Environ. Res. Public Health* **3**, 348–354 (2006).
26. D. A. Butterfield, L. Gu, F. Di Domenico, R. A. Robinson, Mass spectrometry and redox proteomics: Applications in disease. *Mass Spectrom. Rev.* **33**, 277–301 (2014).
27. Q. Xia, *et al*., UVA photoirradiation of benzo[a]pyrene metabolites: Induction of cytotoxicity, reactive oxygen species, and lipid peroxidation. **31**, 898–910 (2015).
28. K. Burke, H. Wei, Synergistic damage by UVA radiation and pollutants. **25**, 219–224 (2009).
29. S. Marzooghi, D. M. Di Toro, A critical review of polycyclic aromatic hydrocarbon phototoxicity models. *Environ. Toxicol. Chem.* **36**, 1138–1148 (2017).
30. A. Roberto, B. S. Larsson, H. Tjälve, Uptake of 7,12-dimethylbenz(a)anthracene and benzo(a)pyrene in melanin-containing tissues. *Pharmacol. Toxicol.* **79**, 92–99 (1996).
31. L. Marrot, Pollution and sun exposure: A deleterious synergy. Mechanisms and opportunities for skin protection. *Curr. Med. Chem.* **25**, 5469–5486 (2018).